Dear Dr. Saverio Mori,

Thank you very much for kindly inviting us to submit a revised manuscript titled "Simulating precipitation radar observations from a geostationary satellite" to Atmospheric Measurement Techniques. We would also appreciate the time and effort you and the reviewers have dedicated to providing insightful feedback on the ways to strengthen our paper.

We would like to submit our revised manuscript. We have incorporated changes that reflect the suggestions you and the reviewers have provided. We hope that the revisions properly address the suggestions and comments.

Sincerely,

A. Okazaki, T. Honda, S. Kotsuki, M. Yamaji, T. Kubota, R. Oki, T. Iguchi, and T. Miyoshi

The reviewer comments are in blue and italic and the replies are in black.

Anonymous Referee #1

The manuscript presents the usefulness of a "feasible" Ku-band precipitation radar for a geostationary satellite (GeoSat/PR). It is an effort ongoing at JAXA to overcome two limitations of orbiting radar-based systems such as TRMM or GPM, namely, the limited swath and revisit time. A geostationary satellite needs a larger antenna than TRMM PR and GPM KuPR. A 20-m antenna for a 20 km footprint is considered in the study for its feasibility. The scan of the radar is within 6° that makes measurements available for a circular disk with a diameter of 8400 km.

Effects of Non Uniform Beam Filling (NUBF) and clutter are presented usng an extremely simple cloud model. The impact of coarse resolutions of the GeoSat/PR is quantified on 3-D Typhoon observations obtained with realistic simulations. The subject of is important and the manuscript is, in general, well written. Therefore it can be recommended for publication. I have some comments and suggestions that should result in a minor revision work for the authors.

1. What is the need of the approximation of equation 4? (moreover, tetab is not defined in the text).

We made the approximation to truncate the edge of the Gaussian function and to confine the calculation domain for Pr and Ps. Nevertheless, we changed the beam pattern from Gaussian to the uniform distribution to consider the impact of sidelobe clutter. We also added the definition of theta_b. Thank you.

2. The model of NRCS of ocean surface does not take into account the modification due to impinging rain. Authors should provide evidence of the fact that this contribution can be neglected.

We appreciate the suggestion. As previous studies show (e.g. Braun et al., 1999; Contreras et al., 2003), the impact of impinging rain is negligible at high wind speed (10 m s^{-1}~). Because the main target of this study is a typhoon which accompanies strong winds, we did not account for the modification due to impinging rain. We included the reason for the assumption of the study in the revised manuscript.

3. Lines 233-234: I guess that the case of a 5 km beamwidth is given provided to make something similar to TRMM PR as reference. The text should better explain why the authors choose the different spatial resolutions. Also the "feasibility" of a 20x20 m antenna should better justified.

We simulated the case with 5 km beam width to see the sensitivity of the result to radar resolution. We included the reason why we show the case in the revised manuscript.

For the latter point, we cited a study by Meguro et al. (2009) and Joudoi et al. (2018) on the feasibility of 20m-by-20m size antenna in the revised manuscript.

4. Lines 350-351: Authors guess that Ku attenuation can be corrected. Do they think that SRT method can be applied with this configuration ? (maybe some references are needed; the same is for sidelobe correction)

We are not sure if the SRT method is applicable to this radar measurement because of its relatively large scattering volume: it is possible that scattering from the surface is not affected by the attenuation because of NUBF. However, development of the attenuation correction method is out of the scope of this study. Therefore, we would like to leave this point for future work. Nevertheless, we added discussion on the impact of the attenuation and the attenuation correction in the revised manuscript. We also included discussion on the sidelobe clutter.

5. Figure 6: please report in the caption that "distance" in the panel is referred to the nadir.

We defined the term "distance" explicitly in the revised manuscript. Thank you.

6. Figure 8, 9, 11, 12: The captions report "Note that the areas where reflectivity form precipitation larger than 0 dBZ are shaded". It is not clear. In figure 9 and 12, close to ground we can see some darker grey that maybe are due to the resolution of the manuscript available to reviewers.

We revised the caption as "Area where reflectivity from precipitation less than 0 dBZ are left blank". To make the point clear, we also modified the figure in the revised manuscript.

7. Figure 8: I suggest to remove wind from panel (a) because it just clutters the "true" reflectivity image.

Removed.

References:

Braun, N., Gade, M., & Lange, P. A., Radar backscattering measurements of artificial rain impinging on a water surface at different wind speeds, paper presented at 1999 International Geoscience and Remote Sensing Symposium (IGARSS), Inst. Of Elect. And Elect. Eng., New York, 1999.

Conteran, R. F., Plant, W. J., Keller, W. C., Hayes, K., & Nystuen, J., Effects of rain on Ku-band backscatter from the ocean, J. Geophys, Res., 108(C5), 3165, 2003.

Joudoi, D., Kuratomi, T., & Watanabe, K., The construction method of a 30-m-class large planar antenna for Space Solar Power Systems, 69th International Astronautical Congress, Bremen, Germany,

1-5, October 2018.

Li, X., He, J., Wang, C., Tang, S., & Hou, X., Evaluation of surface clutter for future geostationary spaceborne weather radar, atmosphere, 8, 14.

Meguro, A., Shintate, K., Usui, M., & Tsujihata, A., In-orbit deployment characteristics of large deployable antenna reflector onboard Engineering Test Satellite VIII, Acta Astronautica, 65(9-10), 1306-1316, 2009.

Anonymous Referee #2

The manuscript "Simulating precipitation radar observations from a geostationary satellite" details a theoretical study of the performance of a hypothetical geostationary weather radar using both a uniform rain layer and more realistic cloud model output. Offering a cogent analysis of the challenges of observing precipitation in the presence of surface clutter due to the coarse resolution of a geostationary platform, the paper is straightforward, well-written, and highly relevant, and should be published after minor revisions.

Specific Comments

There is one point that is really lacking from the discussion: sidelobe clutter. The idealized antenna pattern in the paper neglects antenna sidelobes. Given the attention focused on realistic distributions of precipitation, such analysis can be considered outside of the scope of the paper; however, discussing the results presented in this manuscript in the context of other studies that look at sidelobe clutter (Kubota et al., 2016; Li et al., 2017) would add more depth to the conclusions of the paper.

Thank you for the comments and the helpful references. We included the discussion on the impact of sidelobe clutter and sidelobe clutter correction. Although the impact is not negligible, the correction method proposed by Kubota et al. (2016) should be applicable after a reasonable number of observations are collected.

Technical Corrections

Throughout the paper, "incident" should be "incidence."

Corrected in the revised manuscript.

Lines 44-45: contaminations from the surface clutters -> contamination from surface clutter

Corrected

Line 51: the surface clutters -> surface clutter

Corrected

Line 122: The word "power" should come between "path" and "beam"

Corrected

Line 182: The word "image" after "schematic" is unnecessary.

Removed

Line 227: Include "the" before "Marshall Islands."

Included

Line 228: Remove "the" before "generation."

Removed

Simulating precipitation radar observations from a geostationary satellite

By

Atsushi Okazaki[1], Takumi Honda[1], Shunji Kotsuki[1,2],
Moeka Yamaji[3], Takuji Kubota[3], Riko Oki[3],
Toshio Iguchi[4],
and Takemasa Miyoshi[1,2,5,6,7]

[1]RIKEN Center for Computational Science, Kobe, Japan
[2] RIKEN interdisciplinary Theoretical and Mathematical Sciences Program, Kobe, Japan
[3]Earth Observation Research Center, Japan Aerospace Exploration Agency, Tsukuba, Japan
[4]National Institute of Information and Communications Technology, Koganei, Japan
[5]Department of Atmospheric and Oceanic Science, University of Maryland, College Park,
College Park, Maryland
[6]Japan Agency for Marine-Earth Science and Technology, Yokohama, Japan
[7]Prediction Science Laboratory, RIKEN Cluster for Pioneering Research, Kobe, Japan

To be submitted to the Atmospheric Measurement Techniques

____

Corresponding authors: Atsushi Okazaki and Takemasa Miyoshi, RIKEN Center for
Computational Science, 7-1-26 Minatojima-minami-machi, Chuo-ku, Kobe, Hyogo 650-0047,
Japan (atsushi.okazaki@riken.jp, takemasa.miyoshi@riken.jp)

Abstract

Spaceborne precipitation radars, such as the Tropical Rainfall Measuring Mission (TRMM) and the Global Precipitation Measurement (GPM) Core Observatory, have been important platforms to provide ~~-~~a direct measurement of three-dimensional precipitation structure globally. Building upon the success of TRMM and GPM Core Observatory, the Japan Aerospace Exploration Agency (JAXA) is currently surveying the feasibility of a potential satellite mission equipped with a precipitation radar on a geostationary orbit. The quasi-continuous observation realized by the geostationary satellite radar would offer a new insight into meteorology and would advance numerical weather prediction (NWP) through their effective use by data assimilation.

Although the radar would be beneficial, the radar on the geostationary orbit measures precipitation obliquely at off-nadir points. Besides, the observing resolution will be several times larger than those onboard TRMM and GPM Core Observatory due to the limited antenna size that we could deliver. The tilted sampling volume and the coarse resolution would result in more ~~contaminations~~contamination from ~~the~~ surface ~~clutters~~clutter. To investigate the impact of these limitations and to explore the potential usefulness of the geostationary satellite radar, this study simulates the observation data for a typhoon case using an NWP model and a radar simulator.

The results demonstrate that it would be possible to obtain three-dimensional precipitation data. However, the quality of the observation depends on the beam width, the beam sampling span, and the position of precipitation systems. With a wide beam width and a coarse beam span, the radar cannot observe weak precipitation at low altitudes due to ~~the~~ surface ~~clutters~~clutter. The limitation can be mitigated by oversampling (i.e., a wide beam width and a fine sampling span). With a narrow beam width and a fine beam sampling span, the surface clutter interference is confined to the surface level. When the precipitation system is located far from the nadir, the precipitation signal is obtained only for strong precipitation.

1. Introduction

Knowing the distribution of precipitation in space and time is essential for scientific developments as precipitation plays a key role in global water and energy cycles in the Earth system. Such knowledge is also indispensable to our daily lives and disaster monitoring and prevention. However, observing precipitation globally is not an easy task. Ground-based observations may not adequately represent the rainfall amounts of a broader area since the vast surface of the earth remains unobserved (Kidd et al., 2016). Alternatively, satellites provide an ideal platform to observe precipitation globally. There are three types of methods to observe or estimate precipitation from satellites: visible and infrared, passive microwave, and active microwave (radar). Among them, radar is the most direct method and is the only sensor that can provide three-dimensional structure of precipitation. The first satellite equipped with precipitation radar was the Tropical Rainfall Measuring Mission (TRMM) launched in 1997 (Kummerow et al., 1998; Kozu et al., 2001), and the first satellite-borne dual-frequency precipitation radar onboard the Global Precipitation Measurement (GPM) Core Observatory was launched in 2014 (Hou et al., 2014; Skofronick-Jackson et al., 2017). The observations produced by the precipitation radars onboard the low-earth-orbiting satellites have been contributing to enhance our knowledge on meteorology. For instance, their ability to see through clouds helps understand storm structures (Kelly et al., 2004) and the nature of convection (e.g. Takayabu 2006; Hamada et al., 2015; Houze et al., 2015).

Building upon the success of the TRMM and GPM Core Observatory, the Japan Aerospace Exploration Agency (JAXA) is currently studying the feasibility of a geostationary satellite equipped with precipitation radar (hereafter, simply "~~GeoSat/PR~~GPR"). The main advantage of ~~GeoSat/PR~~GPR over the existing ones with precipitation radar is the observation frequency. Because the previous satellites are low earth orbiters, they cannot observe the same area frequently. For instance, TRMM overpasses a 500 by 500 km^2 box 1-2 times a day on average (Bell et al., 1990). To make the situation worse, it is difficult to capture the whole figure of a large-scale precipitation

82 system (e.g. tropical cyclone) at once due to the narrow scan swath (e.g. 245 km for KuPR on GPM

83 Core Observatory). Alternatively, ~~GeoSat/PR~~GPR stays at the same location all the time and

84 continuously measures precipitation in its range of observation. Those data are expected to help

85 understand important scientific issues. Furthermore, those frequent data could improve the skill of

86 numerical weather prediction (NWP) through data assimilation, leading to more accurate and timely

87 warnings of floods and landslides.

88 Although ~~GeoSat/PR~~GPR would be beneficial, it has potential disadvantages. Since

89 ~~GeoSat/PR~~GPR measures precipitation from the geostationary orbit, it measures precipitation

90 obliquely at off-nadir points. It is unclear how severely this may degrade the observation. In addition,

91 the tilted sampling volume worsens the contamination of the precipitation echo by the surface clutter.

92 Takahashi (2017) showed that the clutter height monotonically increases with the ~~incident~~incidence

93 angle from the wide swath observation during the end-of-mission experiment of the TRMM. The

94 impact of the surface clutter interference with a large ~~incident~~incidence angle would be large if the

95 horizontal resolution of the radar is coarse, and that is the case for ~~GeoSat/PR~~GPR. The horizontal

96 resolution is limited by the antenna size and wavelength. A larger antenna is needed for higher

97 resolution. However, it is challenging to construct a large antenna on a geostationary orbit. ~~Currently~~

98 ~~we consider a 20 m by 20~~The JAXA has launched a satellite with a relatively large antenna of 19 m

99 by 17 m (ETS-VIII, Meguro et al., 2009). Based on the experience and further efforts (Joudoi et al,

100 2018), currently we consider a 30-m-by-30-m square antenna as a feasible choice, whose spatial

101 resolution is 20 km at nadir, that is several times larger than that of TRMM/PR (4.3 km). To

102 investigate the mission feasibility of ~~GeoSat/PR~~GPR, it is important to simulate observation of

103 ~~GeoSat/PR~~GPR and to find its potential usefulness and weakness.

104 In the past decade, a geostationary radar instrument known as the Next Generation Weather Radar

105 (NEXRAD) In Space (NIS; Im et al., 2007) has been proposed. A few studies demonstrated the

106 capability of NIS. Lewis et al. (2011) examined the feasibility of a 35 GHz Doppler radar to observe

107 the wind field. They showed that the direct measurement of winds from the geostationary orbit

108 would be possible for a hurricane case. Li et al. (2017) evaluated the impact of surface clutter for the

109 same radar assuming a uniform rain layer. They showed that most of rain echoes at off-nadir

110 scanning angles will not be contaminated by the surface clutter, when rain intensity is greater than 10

111 mm h^{-1}.

112 However, the impact of the surface clutter and the oblique measurement would depend on the

113 shape and position of the precipitation system. This study extends Li et al. (2017) for a realistic case.

114 By considering the importance to societal and scientific benefit, we chose a typhoon as a test case in

115 this study. We investigate the impact with various typhoon locations and radar parameters such as

116 radar beam width and sampling span for realistic scenarios of a simulated typhoon case.

117 This paper is structured as follows. Section 2 describes the proposed specifications of

118 ~~GeoSat/PR~~GPR and presents the newly-developed radar simulator. Section 3 describes the

119 characteristics of the observation with ~~GeoSat/PR~~GPR for an idealized case. Section 4 presents the

120 results of applying the radar to a typhoon case. Section 5 provides the sensitivity results to the

121 location of the typhoon. Section 6 shows the impact of attenuation and sidelobe clutter. Finally,

122 Section 6 provides conclusions.

123

124 **2. Radar simulator**

125 **2.1. Radar specifications**

126 The specifications of ~~GeoSat/PR~~GPR are summarized in Table. 1. The ~~GeoSat/PR~~GPR is

127 anticipated at 13.6 GHz, the same as KuPR onboard GPM Core Observatory. We assume a

128 ~~20~~30-m-by-~~20~~30-m square phased array radar with the half-power beam width (-3 dB) of 0.032°,

129 with which we can achieve horizontal resolution of 20 km at the nadir point on the earth surface. The

130 range resolution is 500 m. Though shorter-range resolution is technically viable, we adopt this value

131 by considering the balance to the horizontal resolution. The number of the range bins is 60; the

132 corresponding height of the beam center ranges from the surface to 30 km at nadir. The scan angle is

133 ±6°, which covers a circular disk with a diameter of 8400 km on Earth's surface. If ~~GeoSat/PR~~GPR

134 were placed at 135°E of the equator, it would cover from Sumatra to New Caledonia, and from

135 Australia to the southern half of Japan.

136   We assume that the satellite can complete the full disk scan within one hour. In addition to the

137 normal mode, it is expected to have several modes and can observe a targeting precipitation system

138 intensively as in Himawari-8 (Bessho et al., 2016). In this study, we focus only on snap-shots and do

139 not consider the time for ~~GeoSat/PR~~GPR to complete the full disk scan.

140

141 **2.2.   Precipitation reflectivity**

142   This subsection describes how to calculate reflectivity measured by ~~GeoSat/PR (Z_m).~~GPR (Z).

143 First, we convert model hydrometeors (cloud water, cloud ice, rain, snow, and graupel) to ~~reflectivity~~

144 ~~on the~~total backscattering ($\overline{\sigma}_b$) and extinction coefficients ($\overline{k}_{ext}$) at every model grid ~~(Z_e)~~point using

145 an existing software called Joint Simulator for Satellite Sensors (Joint-Simulator; Hashino et al.,

146 2013). The Joint-Simulator is a suite of software that simulates satellite observations based on

147 atmospheric states simulated by cloud-resolving models. ~~The computation of reflectivity in~~

148 ~~Joint-Simulator is based on Masunaga and Kummerrow (2005)~~The total backscattering and

149 extinction coefficients are obtained respectively by summing single-particle backscattering (σ_b^s) and

150 extinction coefficients (k_{ext}^s) for the i th hydrometeor specie following its drop size (D) distribution

151 ($N(D)$) as follows:

$$\text{$\cancel{Z_e = \frac{\lambda^4}{\pi^5|K|^2}\overline{\sigma}_b,}$}\ \overline{\sigma}_b = \sum_{i=1}^{n_{spec}} \int_0^\infty \sigma_{b,i}^s(D)N(D)dD, \tag{1}$$

$$\overline{k}_{ext} = \sum_{i=1}^{n_{spec}} \int_0^\infty k_{ext,i}^s(D)N(D)dD, \tag{2}$$

152 ~~with~~

$$\overline{\sigma}_b = \sum_{i=1}^{5} \int_0^{\infty} \sigma_{b,i}^s(D)N(D)dD, \qquad (2)$$

where ~~λ~~n_{spec} is the ~~wavelength, K the function~~number of the ~~complex reflractivity index of scattering particles, and $\overline{\sigma}_b$ the total backscattering coefficient per unit volume. Following Masunaga and Kummerow (2005), $|K|^2$ is assumed to be a constant (0.925) in this study. The total backscattering coefficients are obtained by summing single particle backscattering (σ_b^s) for the i th hydrometeor specie following its drop size (D) distribution ($N(D)$).~~hydrometeor species. In this study, up to five hydrometeor species, i.e., cloud water, cloud ice, rain, snow, and graupel, were considered. The Mie approximation is ~~assumed~~used to calculate ~~the single particle backscattering~~$\sigma_{b,i}^s$ and $k_{ext,i}^s$ for all ~~the~~ species (Masunaga and Kummerow, 2005).

After calculating ~~the reflectivity on the~~$\overline{\sigma}_b$ and $\overline{k}_{ext}$ at every model grid~~, they~~ point, the grid point values are integrated over the scattering volume following the antenna pattern. The radar-received power from precipitation (P_r) of the beam pointing range r_0 and scan angle θ_0 and ϕ_0 is given by

$$P_r = \frac{P_t\lambda^2}{(4\pi)^3}\int_{r_0-c\tau/4}^{r_0+c\tau/4}\int_{\theta_0-\pi}^{\theta_0+\pi}\int_{\phi_0-\pi/2}^{\phi_0+\pi/2} f^4(\theta,\phi)r^{-2}Z_e(r,\theta,\phi)\,cos\theta\,d\phi\,d\theta\,dr \qquad (3)$$

where P_t is the transmitted power, c the speed of light, τ the pulse duration, and f^4 the two-way effective beam weighting function. ~~Here we~~We assumed the uniform antenna pattern ~~as the Gaussian function, which,~~ whose sidelobe level is ~~approximated by the following fifth order polynomial (Fig. 1; Gaspari and Cohn, 1999):~~ -13.26 dB:

$$f^2(\psi) = \begin{cases} -\frac{1}{4}\psi^5 + \frac{1}{2}\psi^4 + \frac{5}{8}\psi^3 - \frac{5}{3}\psi^2 + 1 & (0 \leq \psi < 1) \\ \frac{1}{12}\psi^5 - \frac{1}{2}\psi^4 + \frac{5}{8}\psi^3 + \frac{5}{3}\psi^2 - 5\psi + 4 - \frac{2}{3}\psi^{-1} & (1 \leq \psi < 2) \\ 0 & (2 \leq \psi) \end{cases}$$

$$f^2(\psi) = \left(\frac{sin\psi}{\psi}\right)^2 \qquad (4)$$

where $\psi = \sqrt{(\theta-\theta_0)^2 + (\phi-\phi_0)^2}/\Psi$, ~~and~~ Ψ is obtained by solving the equation $f\left(\frac{\theta_B}{2}/\right.$

Ψ) f$^2\left(\frac{\theta_B}{2}/\Psi\right) = 0.5$ for Ψ. The, and θ_B is the half-power beam width (-3 dB). $A_P(r, \theta, \phi)$ is the

attenuation factor from the radar reflectivity measured by GeoSat/PR is to range r in the direction of

(θ, ϕ) and calculated as follows:by

$$Z_m = \frac{\int_{r_0-\frac{c\tau}{4}}^{r_0+\frac{c\tau}{4}} \int_{\theta_0-\pi}^{\theta_0+\pi} \int_{\phi_0-\frac{\pi}{2}}^{\phi_0+\frac{\pi}{2}} f^4(\theta,\phi) r^{-2} Z_e(r,\theta,\phi) \cos\theta \, d\phi \, d\theta \, dr}{\int_{r_0-\frac{c\tau}{4}}^{r_0+\frac{c\tau}{4}} \int_{\theta_0-\pi}^{\theta_0+\pi} \int_{\phi_0-\frac{\pi}{2}}^{\phi_0+\frac{\pi}{2}} f^4(\theta,\phi) r^{-2} \cos\theta \, d\phi \, d\theta \, dr} \cdot A_P(r,\theta,\phi) \tag{5}$$

$$= \exp\left[-0.2\ln(10)\int_0^r \bar{k}_{ext}(r',\theta,\phi) dr'\right].$$

The radar reflectivity measured by GPR is calculated as follows:

$$Z = \frac{\lambda^4}{\pi^5 |K|^2} \frac{\int_{r_0-\frac{c\tau}{4}}^{r_0+\frac{c\tau}{4}} \int_{\theta_0-\pi}^{\theta_0+\pi} \int_{\phi_0-\frac{\pi}{2}}^{\phi_0+\frac{\pi}{2}} f^4(\theta,\phi) \bar{\sigma}_b(r,\theta,\phi) A_P(r,\theta,\phi) \cos\theta \, d\phi \, d\theta \, dr}{\int_{r_0-\frac{c\tau}{4}}^{r_0+\frac{c\tau}{4}} \int_{\theta_0-\pi}^{\theta_0+\pi} \int_{\phi_0-\frac{\pi}{2}}^{\phi_0+\frac{\pi}{2}} f^4(\theta,\phi) r^{-2} \cos\theta \, d\phi \, d\theta \, dr}, \tag{6}$$

where λ is the wavelength, K the function of a complex refractivity index of scattering particles. Following Masunaga and Kummerow (2005), $|K|^2$ is assumed to be a constant (0.925) in this study. We do not consider the impact of attenuation ($A_P = 1.0$ everywhere) as it can be corrected with proper methods (e.g. Iguchi et al., 2000) for Sects. 3, 4, and 5.

2.3. Surface clutter

Surface clutter echoes contaminate the precipitation signals. In this study, we assumed that the surface is completely covered by the ocean for simplicity. Radar-received power from the sea surface (P_s) was calculated by

$$P_s = \frac{P_t\lambda^2}{(4\pi)^3}\iint_A \frac{f^4(\theta,\phi)\sigma_0}{r^4} dA \quad P_s = \frac{P_t\lambda^2}{(4\pi)^3}\iint_S \frac{f^4(\theta,\phi)\sigma_0 A_P(r,\theta,\phi)}{r^4} dS \tag{6}\tag{7}$$

where σ_0 is the normalized radar cross section (NRCS) of the ocean surface, and A S the scattering area. We obtained σ_0 using a model proposed by Wentz et al. (1984) based on observations from a microwave scatterometer onboard the Seasat satellite. The model expresses σ_0 as,

$$\sigma_0 = b_0(U_{10})^{b_1} \tag{7}\tag{8}$$

185 where U_{10} is the 10-m wind speed, and b_0 and b_1 are fitted parameters. The NRCS for various

186 wind speed is shown in Fig. ~~2~~2. When raindrops hit the ocean surface, they change the properties of

187 the surface and the scattering signals (Bliven et al., 1997). The impact of impinging rain is negligible

188 at high wind speed (e.g. Braun et al., 1999; Contreras et al., 2003). Since this study focuses on a

189 typhoon case accompanying strong winds, we do not consider the impact of impinging rain. Also, we

190 do not consider the impact of sidelobe clutter as it can be filtered with proper methods (e.g. Kubota

191 et al., 2016) for Sects. 3, 4, and 5.

192

3. Homogeneous case

194 To understand the characteristics of the radar observation, we first show the results from an

195 idealized case, in which we assume the atmosphere below 2 km is uniformly filled with a certain

196 amount of hydrometeor. We tested five cases: 20, 30, 40, 50, and 60 dBZ. The corresponding

197 precipitation intensity is roughly 1, 2, 5, 20, and 60 mm h^{-1} if the hydrometeor consists of only rain.

198 The 10-m wind speed was fixed at 10 m s^{-1} uniformly for all cases. The horizontal resolution of the

199 radar was assumed to be 20 km at the nadir point.

200 Figure 3a shows P_r for the case of 60 dBZ. Two features are apparent in the figure. The first is

201 that the precipitation signal is beyond the precipitation area and becomes taller along with the

202 distance from the nadir, and the second is that P_r decreases monotonically with height. Here and

203 hereafter, the distance was measured along the earth surface.

204 Before discussing the reason for these, first we explain the scattering volume of the

205 ~~GeoSat/PR~~GPR. Here, the scattering volume of the beam pointing range r_0 and scan angle θ_0 and

206 ϕ_0 is defined as the area where r, θ, and ϕ satisfy both $r_0 - \frac{c\tau}{4} \leq r \leq r_0 + \frac{c\tau}{4}$ and ~~$f^2(\psi) > 0$.~~ψ

207 less than the first null point (Fig. 1). Note that sidelobe area is not included in the scattering volume

208 in this section. Figure 4 shows a schematic ~~image~~ of the scattering volume. At the nadir, the

209 ~~incident~~incidence angle is zero, and the scattering volume is nearly parallel to the earth surface (Fig.

Formatted: Indent: First line: 0 ch

210 | 4a). As the ~~incident~~incidence angle increases, the scattering volume becomes tilted against the earth

211 | surface (Fig. 4b). As a result, the upper edge of the scattering volume reaches as high as ~~20~~16 km

212 | when the beam center of the ~~GeoSat/PR~~GPR is at a point 4000 km away from the nadir even in the

213 | lowest range bin (range bin number 1 in Fig. 5b). In the same angle but the highest range bin, the

214 | scattering volume ranges from ~~2~~4 km to ~~44~~38 km in height (range bin number 60 in Fig. 5b). The

215 | range of the scattering volume is even larger with sidelobe area.

216 | When the beam center is at the level higher than the precipitating area, there is no precipitation

217 | around the beam center. On the other hand, the tip of the scattering volume may touch the

218 | precipitating area with the tilted scattering volume at off-nadir. In such a case, the scattering volume

219 | is not fully filled with precipitation. Such nonuniform beam filling (NUBF) results in the reduction

220 | of P_r with ~~Z_e~~$\bar{\sigma}_b = 0$ in the upper part of the volume compared with the fully filled case. Although

221 | the value is small, still ~~GeoSat/PR~~GPR catches the signal of precipitation, and thus P_r has a value

222 | even when the beam center is at the point higher than the precipitating area. As the scattering volume

223 | becomes more tilted against the earth surface along with the distance from the nadir (Fig. 5a), the

224 | maximum height at which the beam gets a signal from precipitation becomes higher along with the

225 | distance from the nadir. Hence, we have the signal beyond the precipitation area and the area

226 | becomes taller along with the distance from the nadir.

227 | The P_r magnitude dependence on the height is also explained by the NUBF. Due to the

228 | experimental setting where precipitation exists only in the atmosphere below 2 km, the beam with

229 | the scattering volume touching the level higher than 2 km ~~are~~is not fully filled with precipitation.

230 | The higher the ~~GeoSat/PR~~GPR observes, the less the scattering volume is filled with precipitation.

231 | Accordingly, P_r decreases with height.

232 | The pattern of P_s is similar to that of P_r, showing dependence on the distance from the nadir (Fig.

233 | 3b) because σ_0 is a function of the ~~incident~~incidence angle (Fig. 2).

234 | Figure 6 shows signal-to-clutter ratio (SCR) defined as P_r/P_s (dB). The larger SCR, the less

235   contaminated by the clutter. In the figure, areas where the reflectivity from precipitation exceeds 0

236   dBZ are shaded. For all the cases, SCR is the largest at nadir and high altitudes. The minimum SCR

237   is found at the surface level around 500 km away from the nadir reflecting the peak of the echo from

238   the surface clutter. As expected, SCR becomes large when precipitation is strong since the received

239   power from the precipitation becomes larger while P_s is the same for all the cases. The

240   ~~GeoSat/PR~~GPR can perceive precipitation only at the nadir point and high altitudes in the case of 20

241   dBZ (Fig. 6a), but SCR is larger than zero over the whole precipitating area in the case of 60 dBZ

242   (Fig. 6e) except for the surface level in 0 to 1000 km away from the nadir. The comparison of the

243   two cases also suggests that the surface clutter contaminates the precipitation signal from high

244   altitudes for weak precipitation. On the other hand, if the precipitation is strong enough, the clutter

245   interference is ~~very~~ limited, and we should get the signal even at the surface level.

246   The simulated results are consistent with Takahashi (2017) and Li et al. (2017), suggesting that

247   both results be plausible.

248

249   **4.   Typhoon case**

250   Section 3 presented the characteristics of reflectivity of ~~GeoSat/PR~~GPR. However, what we can

251   observe will depend on the size and structure of the target precipitation system. To investigate the

252   capability of ~~GeoSat/PR~~GPR in detail, we ran an atmospheric model and applied the radar simulator

253   to produce synthetic observations of reflectivity. As an example, we chose Typhoon Soudelor in 2015,

254   which was the strongest typhoon in that year. Soudelor, generated on 1 August 2015 around the

255   Marshall Islands, rapidly intensified to Super Typhoon equivalent to Category 5 Hurricane within 24

256   hours from ~~the~~ generation and dissipated on 11 August 2015. In this study, we focused on the mature

257   stage of Soudelor at 0000 UTC 5 August 2015.

258   In this section, we focus on the sensitivity to two radar parameters: beam width and beam

259   sampling span. Three cases were examined: the first adopts the beam width and sampling span of 20

km, the experiment named "bw20bs20~."". The second ~~uses the 5 km beam width and span (bw05bs05), and the third~~ uses 20-km resolution of beam width, but the beam span is chosen to be 5 km (bw20bs05), representing an over-sampling case. ~~The~~The third uses the 5-km beam width and span (bw05bs05). Although it is unrealistic to assume a radar with the 5-km beam width at this moment, exploring what kind of observations we can get with the 5-km beam width would be beneficial for the antenna design in the future. The radar settings are summarized in Table 2.

4.1. SCALE-RM simulation

We used a regional cloud-resolving model, SCALE-RM version 5.0.0 (Nishizawa et al., 2015; Sato et al., 2015) to simulate Soudelor. SCALE-RM is based on the SCALE library for weather and climate simulations. The source code and documents of the SCALE library including SCALE-RM are publicly available at http://r-ccs-climate.riken.jp/scale/. The moist physical process is parameterized by a 6-class single-moment bulk microphysics scheme (Tomita et al., 2008), and the five species of hydrometeors (rain, cloud water, cloud ice, snow, and graupel) were used to calculate the radar reflectivity. We use the level-2.5 closure of the Mellor–Yamada–Nakanishi–Niino turbulence scheme to represent subgrid-scale turbulences (Nakanishi and Niino 2004). For shortwave and longwave radiation processes, the Model Simulation Radiation Transfer code (MSTRN) X (Sekiguchi and Nakajima, 2008) is used. See http://r-ccs-climate.riken.jp/scale/ for more detail.

We performed an offline nesting simulation. The horizontal grid spacings and the number of vertical levels for the outer (inner) domain were 15 km (3 km) and 36 levels (56 levels), respectively. Hereafter, the simulation for the outer (inner) domain is referred to as D1 (D2) (Fig. 7a). The initial and lateral boundary conditions for D1 were taken from the National Centers for Environmental Prediction (NCEP) Global Forecasting System (GFS) operational analyses at 0.5° resolution every 6 hour. The initial and lateral boundary conditions for D2 were taken from D1. The simulation covers the period from 0000 UTC 28 July 2015 (0000 UTC 28 July 2015) to 0000 UTC 9 August 2015

285   (0000 UTC 7 August 2015) for D1 (D2).

286   Figure 7 shows the Soudelor's track and minimum sea level pressure (MSLP) at the typhoon

287   center from the best track of the Japan Meteorological Agency (JMA) and the D1 and D2 simulations.

288   The JMA best track shows a rapid decrease of MSLP during the three days from 1 August. D1

289   captures the rapid intensification while D2 shows a slightly slower intensification than the best track.

290   As for the track, both D1 and D2 closely follow the best track albeit slightly shifted northward. We

291   used D2 as a reference to simulate radar observations.

292

293   **4.2. Results**

294   Figures 8 and 9 show radar reflectivity near the surface level and its vertical cross section in a

295   mature stage of the simulated Soudelor (0000 UTC 5 August 2015). The results are shown in the

296   longitude-latitude coordinate for Fig. 8 (a) and in the scan-angle coordinate of the ~~GeoSat/PR~~GPR

297   for Fig. 8 (b-d) covering the same domain as Fig. 8 (a). As in the homogeneous case, areas where the

298   reflectivity from precipitation exceeds 0 dBZ are shaded by grey.

299   Figure 8 (a) and 9 (a) show the reflectivity of the full-resolution nature run for reference. The

300   figures show the typical structure of a tropical cyclone characterized by no rainfall within the eye,

301   heavy rainfall in the eye wall, and the spiral outer-rainband structure.

302   The bw20bs20 captures the spatial distribution well but without fine structures. The difference is

303   noticeable in the outer rainband (gray-colored area) in which the shape of the bands is different from

304   the reference. With the tilted and relatively large scattering volume, the radar catches the signal of

305   precipitation that is in the level higher than the level shown in the figure. The bw20bs20 also misses

306   the local maxima of precipitation. For instance, the strongest precipitation south of the eye (red area

307   in Fig. 8a) was not well captured by bw20bs20. This is because the echo from sharp and strong

308   precipitation was averaged out due to NUBF within the relatively large scattering volume. For the

309   vertical cross-section, the observation roughly captures the structure albeit in a jaggy and discretized

310 manner because of the tilted and relatively large scattering volume (Fig. 9b). The tilted scattering

311 volume also results in the precipitation echo taller than the reference as discussed in Sect. 3.

312 On the other hand, the satellite observes precipitation accurately for both spatial and vertical

313 cross-sections in bw05bs05 (Fig. 8d and Fig. 9d).

314 In the case of bw20bs05 (i.e. oversampling case), the radar inherited the shortcomings in

315 bw20bs20 due to the wide beam width: the larger precipitated area in the outer rainband (Fig. 8c) and

316 taller precipitation pattern (Fig. 9c) compared with the reference. On the other hand, the results were

317 arguably improved thanks to the fine sampling span compared with bw20bs20. For instance, the

318 strong precipitation south of the eye was well captured compared with bw20bs20 (Fig. 9c).

319 Furthermore, individual convective cells south of the typhoon were observed as individual cells

320 although they were blurred due to NUBF within the large scattering volume. This is because the finer

321 sampling span increased the probability for the beam center to hit the area of heavy rainfall.

322 To compare the skills quantitatively, we computed the threat scores with a threshold of 20, 30, 40,

323 and 50 dBZ for all the experiments. Figure 10 shows that bw05bs05 is the best and also shows the

324 benefit of oversampling. Namely, the score of bw20bs05 increased by more than 20 % on average for

325 all the thresholds compared with that of bw20bs20.

326 Figures 9 and 10 also shows the impact of the surface clutter. The hatched area in Fig. 9 shows the

327 area where SCR is less than or equal to zero. Assuming that the SCR of zero is the minimum

328 threshold to indicate whether the clutter interference will be serious (Li et al., 2017), the hatched area

329 is considered as unobservable. The unobservable area was confined up to 3-km in bw05bs05, while

330 they reached as high as 7 km in bw20bs20 and bw20bs05. Thus, to reduce the impact of the surface

331 clutter, the beam width needs to be narrow enough.

332

333 **5. Dependence on the position of typhoon**

334 At other than the nadir point, the radar observes precipitation obliquely and consequently the

precipitation echo is easy to be contaminated by the surface clutter. As mentioned in Sect. 3, how severely surface clutter contaminates the precipitation echo depends on the ~~incident~~incidence angle of the beam, which corresponds to the distance from the nadir. Therefore, the location of the target precipitation system should have an impact on the quality of the observations. This section investigates the sensitivity to the location of the typhoon.

We used the simulated Typhoon Soudelor as the reference as in Sect. 4. We picked out the mature stage of the typhoon whose center is in 18° N, 136° E as an example and moved it north and south to represent typhoons whose center is in 10° N, 20° N, and 30° N. We assumed the longitudinal position of the typhoon centers were the same as the sub-satellite point for all the cases to compare the difference originating from the latitudinal position of the typhoon center. The radar used in this section was the same as the one in the bw20bs05.

Figure 11 shows the precipitation echo at the near surface level for the three cases together with the reference. Among them, the precipitation pattern in 10° N was the most similar to the reference, and the threat score was the highest (Fig. 13). As the typhoon position is away from the sub-satellite point, the precipitation is observed weaker with the outer-rainband area more expanded, and the threat score becomes lower (Fig. 13). As discussed in the previous sections, those are due to the widely tilted scattering volume with which the beam captures the signal of precipitation in high altitude whose intensity is weaker than that in the level shown (cf. Fig. 12). The tilted scattering volume also resulted in vertically extended precipitation echo (Fig. 12). The further away from the nadir, the more vertically extended the precipitation echo. This is also true for the clutter height (SCR ≤ 0): the further away from the nadir, the higher the clutter height. However, this is only the case for the area with weak precipitation. In the area with heavy precipitation at a higher latitude, the impact of the surface clutter is limited to the near surface level. For instance, the strongest precipitation in the south of the eye is not affected by the surface clutter at all in the case of 30° N (Fig. 12d), while those are masked by the clutter in the cases of 10° N and 20° N (Fig. 12b and 12c).

Those results are also evident in the threat score (dashed line in Fig. 13). The surface clutter is determined by cross section σ_0 integrated over the scattering area A, and both σ_0 and A decrease along with the ~~incident~~incidence angle in this area. Therefore, the echo from the sea surface clutter becomes smaller and SCR becomes larger along with the latitude.

We obtained the similar results as shown in Sect. 3 with the typhoon case. When the observation target is in low latitude (i.e. close to the nadir), the clutter height is low, and the radar can observe weak precipitation free from clutter at high altitudes. It should be difficult to observe precipitation at the near surface level, even if the precipitation is strong. In case the radar observes precipitation in mid-latitudes (i.e. away from the nadir), the radar cannot observe weak precipitation at most of the altitude while it is easier to observe strong precipitation at any altitude.

6. Impact of attenuation and sidelobe clutter

In the previous sections, we did not consider the impact of attenuation and sidelobe clutter, assuming that they can be corrected (e.g. Iguchi et al., 2000) or filtered (e.g. Kubota et al., 2016). In this section, we investigate the impact of attenuation and sidelobe clutter. To consider attenuation, the attenuation coefficient is included in the calculation of P_r, P_s, and Z (Eqs. 3, 6, and 7). The attenuation coefficients are calculated with Eq. (5), and the extinction coefficients are calculated by Joint-Simulator (Hashino et al., 2013). To investigate the impact of sidelobe clutter, the observation volume is expanded to include the sidelobe area up to the fifth null point (Fig. 1).

Figure 14 shows the cross-section of the typhoon with various radar parameters; bw20bs20, bw20bs05, and bw05bs05. Due to the attenuation, reflectivity from heavy rain is weakened for all the cases (c.f. the reflectivity at south of the eye). This feature is also evident in the threat score for the case with bw20bw05 (Fig. 15). Figure 15 compares three cases: The first case ("main") does not consider the impact of attenuation, and its observation volume does not include sidelobe area, i.e., the same as the bw20bs05 in Fig. 10. The second case ("main+side") does not consider the impact of

attenuation, but its observation volume includes sidelobe area, i.e., considering the impact of sidelobe clutter. The third case ("main+atten.") considers the impact of attenuation, but its observation volume does not include the sidelobe area. Figure 15 shows that the threat score of "main+atten." is almost identical to that of "main" and the impact of attenuation is negligible with the thresholds of 20, 30, and 40 dBZ. On the other hand, the threat score of "main+atten." with the threshold of 50 dBZ is zero at all heights. Therefore, the attenuation makes it difficult to obtain rain echoes from strong precipitation.

On the other hand, the sidelobe clutter contaminates the weak to moderate rain echoes. For example, the top of convection at around 17°N is masked by the sidelobe clutter for the cases with low resolution beam (Figs. 14a and 14b). Figure 15 also shows that threat scores of "main+side" are smaller than that of "main" for the thresholds of 20, 30, and 40 dBZ while the impact is negligible with the threshold of 50 dBZ. Therefore, the sidelobe clutter contaminates weak to moderate rain.

6.7. Summary

We examined the feasibility of radar observation for precipitation from a geostationary satellite. The results demonstrated that it would be possible to obtain three-dimensional precipitation data. However, the quality of the observation was found to depend on the beam width, the beam sampling span, and the position of targeting precipitation systems. With the wide beam width and coarse beam span, the radar cannot observe weak precipitation at low altitudes. The limitations can be somewhat mitigated by oversampling (i.e., a wide beam width but a fine sampling span). With the narrow beam width and fine beam sampling span, the surface clutter interference was confined to the surface level. For the position of the target precipitation system, the larger (smaller) the off-nadir angle, the easier (more difficult) it is to obtain the precipitation signal if the precipitation is strong (weak).

In thisThis study, we did not consider also investigated the impact of attenuation, assuming that it can be corrected (e.g. and sidelobe Iguchi et al., 2000). Also, we assumed that the area where SCR

is greater than zero is observable, assuming that the clutter filter would be available. Therefore, an. The attenuation hinders to obtain rain echoes from strong precipitation while the sidelobe clutter contaminates signals from weak precipitation. An attenuation correction method like the surface-reference method (e.g. Iguchi et al., 2000; Meneghini et al., 2000) and a clutter filter should be developed in the future(e.g. Kubota et al., 2016) must be devised to mitigate the detrimental impacts. One possible idea for the filter may be to distinguish an echo from precipitation and surface by using Doppler shift, but this remains to be a subject of future research.

If the wide beam width of 0.032° is used, the raw product may be prohibitively coarse for a specific purpose. One possible way to effectively downscale such observations is to assimilate the data for NWP. By doing this, the information can be treated properly, and we can get precipitation information in the prediction model coordinate. However, it is not trivial whether assimilation of such data is useful for NWP. In the future, an observing system simulation experiment (OSSE) will be conducted using precipitation measurements simulated with the simulator developed in this study to evaluate the potential impacts of the GeoSat/PRGPR on NWP. Given that wind field observation may be possible from a geostationary satellite as shown in Lewis et al. (2011), the combined use of both observations would be an attractive option.

Acknowledgement

This study was partly supported by the Japan Aerospace Exploration Agency (JAXA); and the FLAGSHIP2020 Project of the Ministry of Education, Culture, Sports, Science and Technology Japan. The experiments were performed using the K computer at the RIKEN R-CCS (ra000015, hp160229, hp170246, hp180194).

Reference

Bessho, K., Date, K., Hayashi, M., Ikeda, A., Imai, T., Inoue, H., Kumagai, Y., Miyakawa, T., Murata, H., Ohno, T., Okuyama, A., Oyama, R., Sasaki, Y., Shimazu, Y., Shimoji, K., Sumida, Y., Suzuki, M., Taniguchi, H., Tsuchiyama, H., Uesawa, D., Yokota, H., Yoshida, An introduction to Himawari-8/9: Japan's new-generation geostationary meteorological satellites, J. Meteorol. Soc. JPN., 94, 151‑183, 2016.

Bliven, L. F., Sobieski, P. W., and Craeye, C., Rain generated ring-waves: Measurements and modelling for remote sensing, Int. J. Remote. Sens., 18, 221-228, 1997.

Braus, N., Gade, M., and Lange, P. A., Radar backscattering measurements of artificial rain impinging on a water surface at different wind speeds, paper presented at 1999 International Geoscience and Remote Sensing Symposium (IGARSS), Inst. of Elect. and Elect. Eng., New York, 1999.

Cho, H.-K., Bowman, P. B., and North, G. R., Equatorial waves including the Madden-Julian Oscillation in TRMM rainfall and OLR data, J. Climate, 17, 4387-4406, 2004.

Contreras, R. F., Plant, W. J., Keller, W. C., Hayes, K., and Nystuen, J., Effects of rain on Ku-band backscatter from the ocean, J. Geophys. Res., 108, C5,3165, 2003.

Gaspari, G., and Cohn, S., Construction of correlation functions in two and three dimensions, Q. J. Roy. Meteor. Soc., 125, 723-757, 1999.

Hashino, T., Satoh, M., Hagihara, Y., Kubota, T., Matsui, T., Nasuno, T., and Okamoto, H., Evaluating cloud microphysics from NICAM against CloudSat and CALIPSO, J. Geophys. Res. Atmos., 118, 7273-7292, 2013.

Hamada, A., Takayabu, Y. N., Liu, C., and Zipser, E. J., Weak linkage between the heaviest rainfall and tallest storms, Nat. Commun, doi: 10.1038/ncomms7213, 2015.

Hou, A. Y., R. K. Kakar, S. Neeck, A. A. Azarbarzin, C. D. Kummerow, M. Kojima, R. Oki, K. Nakamura, and T. Iguchi, 2014: The global precipitation measurement mission. Bull. Amer. Meteor. Soc., 95, 701-722.

Houze, R. A., Rasmussen, K. L., Zuluaga, M. D., and Brodzik, S. R., The variable nature of convection in the tropics and subtropics: A legacy of 16 years of the Tropical Rainfall Measuring Mission satellite, Rev. Geophys., 53, 994-1021, 2015.

Iguchi, T., Kozu, T., Meneghini, R., Awaka, J., Okamoto, K., Rain-profiling algorithm for the TRMM precipitation radar, J. Appl. Meteorol., 39, 2038-2052, 2000.

Im, E., Smith, E. A., Chandrasekar, V. C., Chen, S., Holland, G., Kakar, R., Tanelli, S., Marks, F., and Tripoli, G., Workshop report on NEXRAD-In-Space -A geostationary satellite doppler weather radar for hurricane studies, 33rd Conf. on Radar Meteorology, Cairns, QLD, Australia, Amer. Meteor. Soc., 4B.5, 2007 [Available online at http://ams.confex.com/ams/pdfpapers/123726.pdf.].http://ams.confex.com/ams/pdfpapers/123726.pdf.].

Joudoi, D., Kuratomi, T., and Watanabe, K., The construction method of a 30-m-class large planar

472 antenna for Space Solar Power Systems, 69th International Astronautical Congress, Bremen,
473 Germany, 1-5, October 2018.

474 Kelley, O. A., Stout, J., and Halverson, J. B., Tall precipitation cells in tropical cyclone eyewalls are
475 associated with tropical cyclone intensification, Geophys. Res. Lett., 31, L24112, 2004.

476 Kidd, C., Becker, A., Huffman, G. J., Muller, C. L. Joe, P., Skofronick-Jackson, G., and Kirschbaum,
477 D. B., So, how much of the earth's surface is covered by rain gauges?, B. Am. Meteorol, Soc.,
478 doi: 10.1175/BAMS-D-14-00283.1, 2016.

479 Kozu, T, T. Kawanishi, H. Kuroiwa, M. Kojima, K. Oikawa, H. Kumagai, K. Okamoto, M. Okumura,
480 H. Nakatshka, and K. Nishikawa, Development of precipitation radar onboard the Tropical
481 Rainfall Measuring Mission (TRMM) satellite. IEEE Trans. Geosci. Remote Sens., 39, 102-116,
482 2001.

483 Kubota, T., Iguchi, T., Kojima, M., Liao, L., Masaki, T., Hanado, H., Meneghini, R., and Oki, R., A
484 statistical method for reducing sidelobe clutter for the Ku-band precipitation radar on board the
485 GPM Core Observatory, J. Atmos. Oceanic Technol., 33, 1413-1428, 2016.

486 Kummerow, C., W. Barnes, T. Kozu, J. Shiue, and J. Simpson, The Tropical Rainfall Measuring
487 Mission (TRMM) sensor package, J. Atmos. Oceanic Technol., 15, 808--816, 1998.

488 Lewis, W. E., Im, E., Tanelli, S., Haddad, Z., Tripoli, G. J., Smith, E. A., Geostationary doppler radar
489 and tropical cyclone surveillance, J. Atmos. Ocean. Tech., 28, 1185-1191, 2011.

490 Li, X., He, J., Wang, C., Tang, S., Hou, X., Evaluation of surface clutter for future geostationary
491 spaceborne weather radar, Atmosphere, 8, 14, doi: 10.3390/atmos8010014, 2017.

492 Kubota, T., Shige, S., Hashizume, H., Aonashi, K., Takahashi, N., Seto, S., Hirose, M., Takayabu, Y.
493 N., Ushio, T., Nakagawa, K., Iwanami, K., Kachi, M., Okamoto, K., Global precipitation map
494 using satellige-borne microwave radiometers by the GSMaP Project: Production and validation,
495 IEEE T. Geosci. Remote., 45, 7, 2259-2275, 2007.

496 Masunaga, H., and Kummerow, C., Combined radar and radiometer analysis of precipitation profiles
497 for a parametric retrieval algorithm, J. Atmos. Ocean. Tech., 22, 909-929, 2005.

498 Meguro, A., Shintate, K., Usui, M., and Tsujihata, A., In-orbit deployment characteristics of large
499 deployable antenna reflector onboard Engineering Test Satellite VIII, Acta Astronautica,
500 65(9-10), 1306-1316, 2009.

501 Meneghini, R., Iguchi, T., Kozu, T., Liao, L., Okamoto. K., Jones, J. A., and Kwiatkowski, J., Use of
502 the surface reference technique for path attenuation estimates from the TRMM radar, J. Appl.
503 Meteorol., 39, 2053-2070, 2000.

504 Morita, J., Takayabu, Y. N., Shige, S., Kodama, Y., Analysis of rainfall characteristics of the
505 Madden-Julian oscillation using TRMM satellite data, Dynam. Atmos. Oceans, 42, 207-126,
506 2006.

507 Nakanishi, M., and Niino, H., An improved Mellor–Yamada level-3 model with condensation
508 physics: Its design and verification, Bound.-Lay. Meteorol., 112, 1–31, 2004.

509 Okamoto, K., Aonashi, K., Kubota, T., Tashima, T., Experimental assimilation of the GPC Core

Observatory DPR reflectivity profiles for Typhoon Halong (2014), Mon. Weather Rev., 144, 2307-2326, 2016.

Otsuka, S., Kotsuki, S., Miyoshi, T., Nowcasting with data assimilation: A case of global satellite mapping of precipitation, Weather Forecast., 31, 1409-1416, 2016.

Sekiguchi, M., and Nakajima, T., A k-distribution-based radiation code and its computational optimization for an atmospheric general circulation model, J. Quant. Spectrosc. Ra.,J. Quant. Spectrosc. Radiat. Transfer, 109, 2779–2793, 2008.

Skofronick-Jackson, G., Petersen, W. A., Berg, W., Kidd, C., Stocker, E. F., Kirschbaum, D. B., Kakar, R., Braun, S. A., Huffman, G. J., Iguchi, T., Kirstetter, P. E., Kummerow, C., Meneghini, R., Oki, R., Olson, W. S., Takayabu, Y., Furukawa, K., Wilheit, T., The global precipitation measurement (GPM) mission for science and society, B. Am. Meteorol. Soc., 98, 1679-1695, 2017.

Takahashi, N., Surface echo characteristics derived from the wide swath experiment of the precipitation radar onboard TRMM satellite during its end-of-mission operation, IEEE T. Geosci. Remote., 55, 4, 1988-1993, 2017.

Takayabu, Y. N., Rain-yield per flash calculated from TRMM PR and LIS data and its relationship to the contribution of tall convective rain, Geophys. Res. Lett., 33, L18705, 2006.

Tomita, H., New microphysical schemes with five and six categories by diagnostic generation of cloud ice, J. Meteorol. Soc. JPN., 86A, 121-142, 2008.

Wentz, F. J., Peteherych, S., Thomas, L. A., A model function for ocean radar cross sections at 14.6 GHz, J. Geophys. Res., 89, c3, 3689-3704, 1984.

532 **Tables**

533

534 **Table 1** Specifications of the precipitation radar aboard geostationary satellite

Parameter	Value
Frequency	13.6GHz
Scan angle	±6°
Range resolution	≤500m
Horizontal resolution	20km at nadir
Observation range	30km at nadir

535

536 **Table 2** Radar settings. The figures show the resolution at the nadir point.

Experiment	Beam width	Beam span
bw05bs05	5km	5km
bw20bs05	20km	5km
bw20bs20	20km	20km

537

538

539   **Figures**

540

541

542
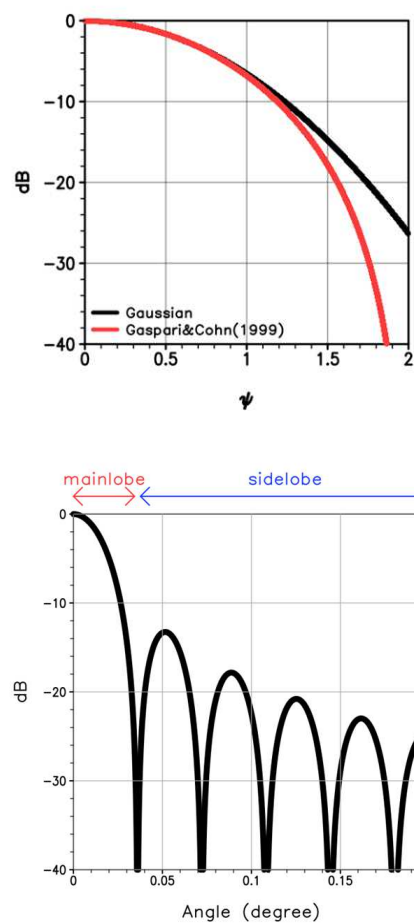
543   **Figure 1** Beam pattern (dB) as a function of ~~normalized~~ beam direction angle. ~~Black and red curves~~

544   ~~show the Gaussian function and the fitted fifth order polynomial (Gaspari and Cohn, 1999),~~

545   ~~respectively.~~ (degree).

546

547
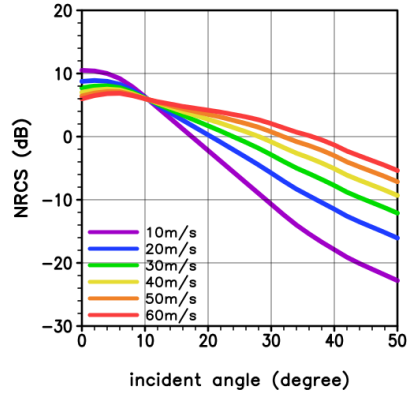
Figure 2 Normalized radar cross section (dB) as a function of ~~incident~~incidence angle for six cases

549   of 10-m wind speed.

550
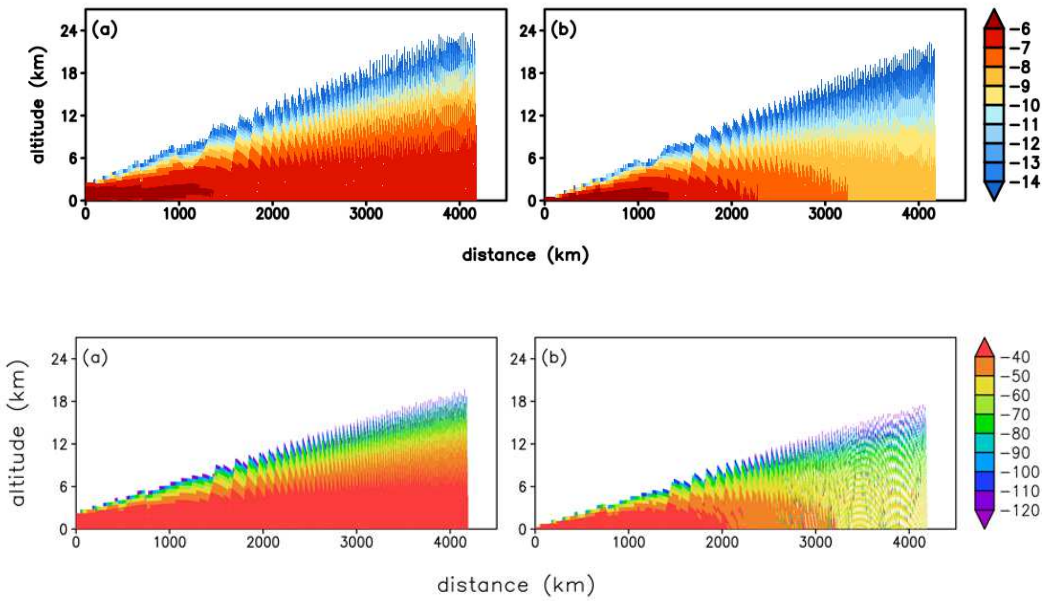
553   **Figure 3** Received power from (a) precipitation, and (b) sea surface clutter, normalized by P_t (dB).

554

(a) nadir   (b) off-nadir

555
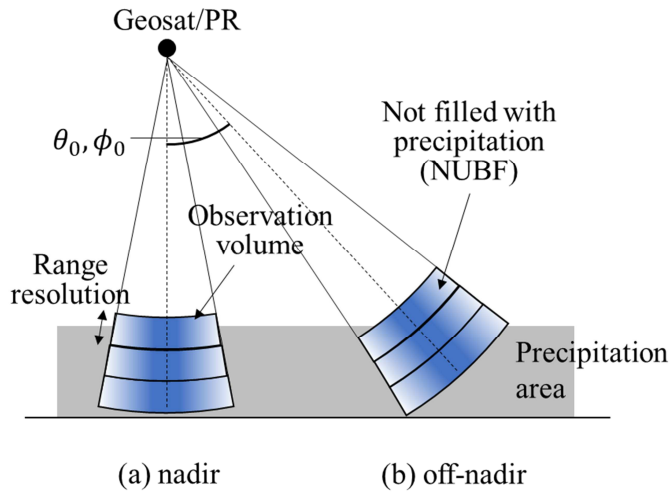
556   **Figure 4** Schematic image of the scattering volume at (a) nadir, and (b) off-nadir.

557
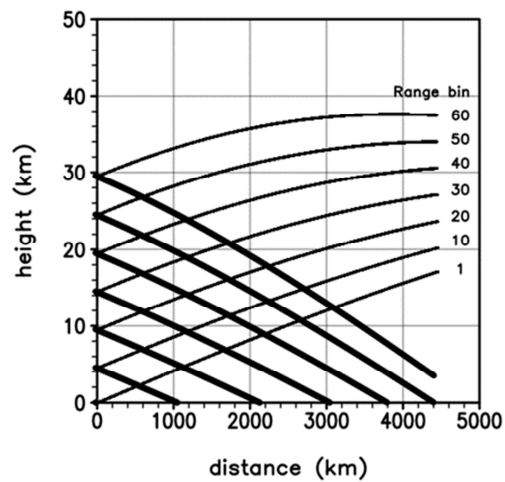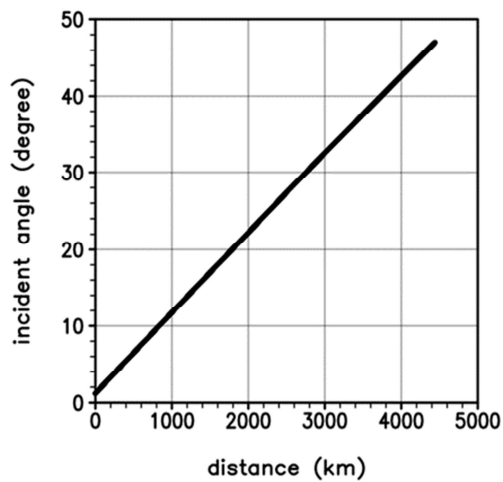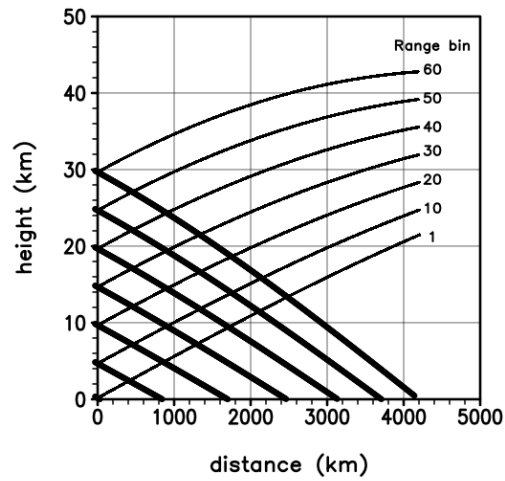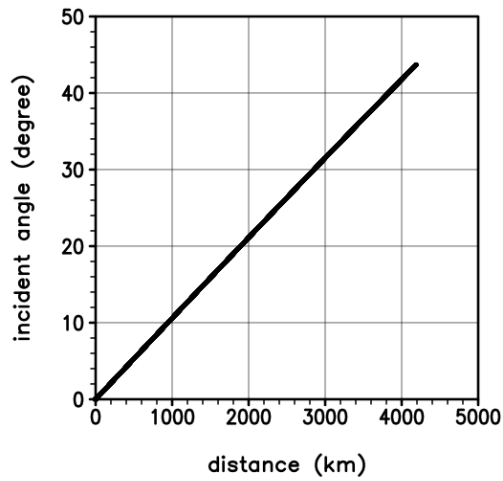
Figure 5 ~~Incident~~Incidence angle (a) and height of the radar scattering volume (b) as a function of the distance from the nadir. Thick and thin lines in (b) shows the lower and upper bound, respectively.

564

565
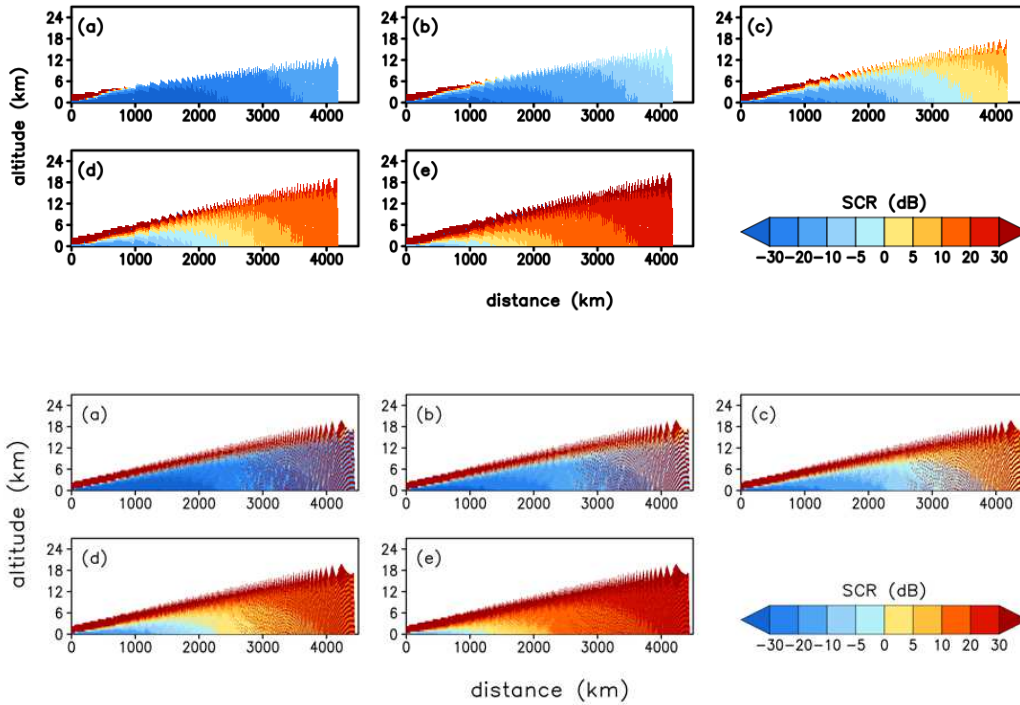
Figure 6 Signal-to-clutter ratio (SCR) in measuring five precipitation intensity (a) 20, (b) 30, (c) 40, (d) 50, and (e) 60 dBZ, as a function of the distance from the nadir (km). It is assumed that the altitude lower than 2 km is filled with homogeneous precipitation.

569
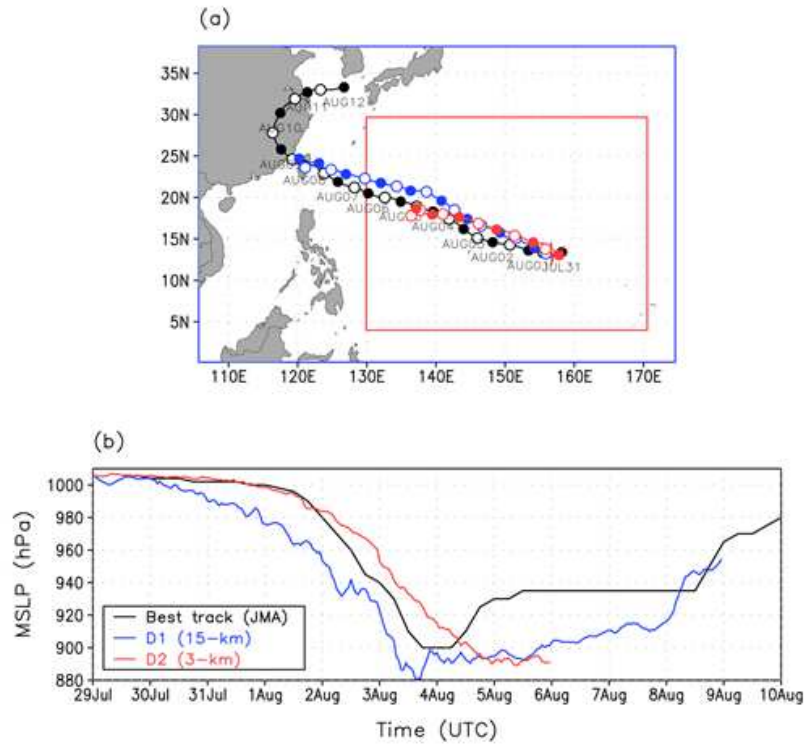
570

571 **Figure 7** (a) Model domains for D1 (blue) and D2 (red) and typhoon tracks, and (b) time series of

572 minimum sea level pressure (MSLP). Black, blue, and red colors show the JMA best track data, D1

573 simulation, and D2 simulation, respectively. Closed and open circles in (a) denote the typhoon

574 positions at 0000 UTC and 1200 UTC, respectively.

575

576

577
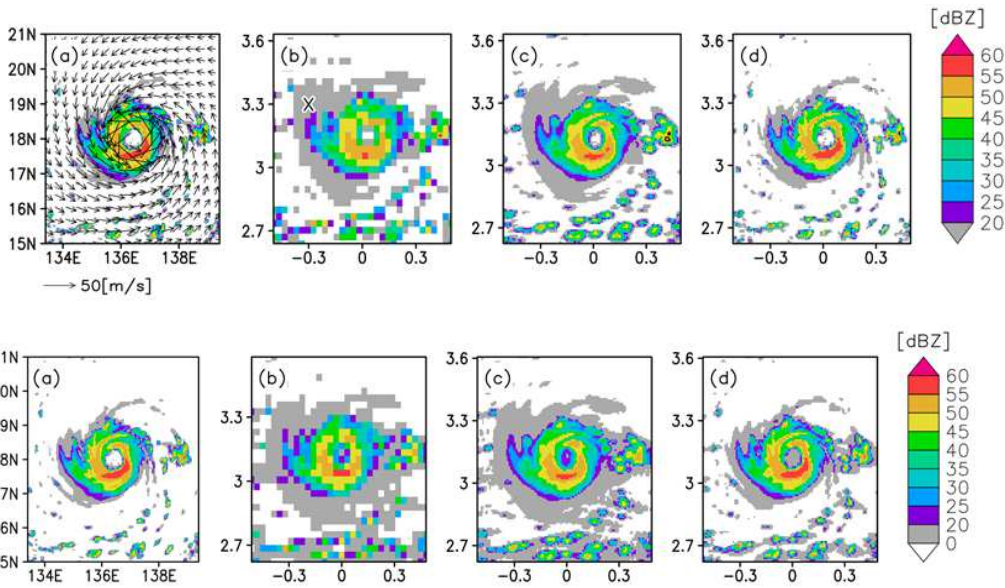
578 **Figure 8** Radar reflectivity (dBZ) near the surface in the typhoon mature stage (0000 UTC, 5 August

579 2015) for (a) the truth, (b) bw20bs20, (c) bw20bs05, and (d) bw05bs05. 10-m wind speed is overlaid

580 in (a). ~~Note that the areas~~The area where reflectivity ~~form~~from precipitation ~~larger~~less than 0 dBZ

581 are ~~shaded~~left blank.

582

583
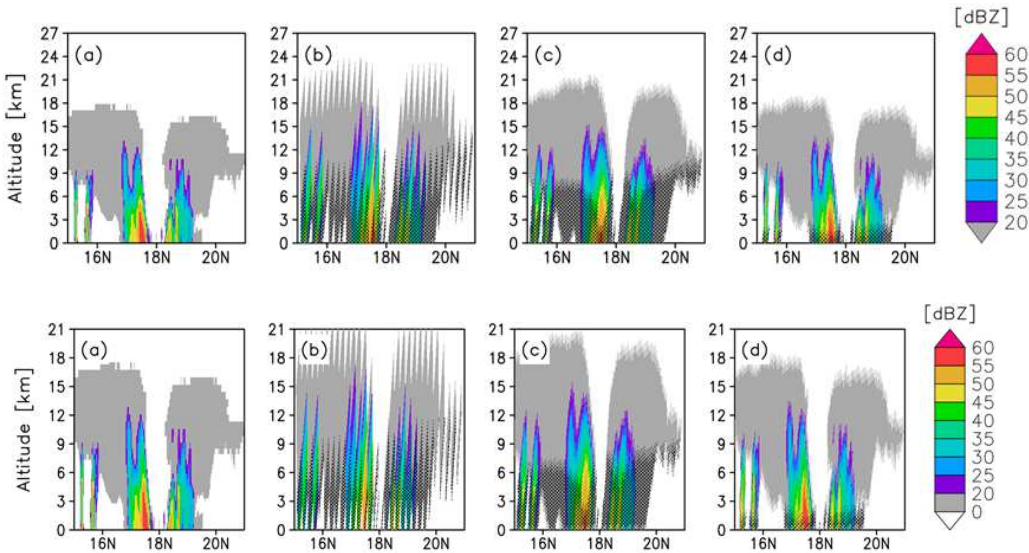
584 **Figure 9** Precipitation reflectivity (dBZ) along 136.4°E longitude line passing through the typhoon

585 center in the mature stage (0000 UTC, 5 August 2015) for (a) the truth, (b) bw20bs20, (c) bw20bs05,

586 and (d) bw05bs05. The area ~~in which SCR < 0 is hatched in (b-d). Note that the areas~~ where

587 reflectivity ~~form~~from precipitation ~~larger~~less than 0 dBZ are ~~shaded.~~left blank and the area in which

588 SCR < 0 is hatched in (b-d).

589

590

591 **Figure 10** Threat score with a threshold of (a) 20, (b) 30, (c) 40, and (d) 50 (dBZ) for bw20bs20

592 (red), bw20bs05 (green), and bw05bs05 (blue). The dotted and solid lines show the threat score with

593 and without considering the impact of surface clutter, respectively.
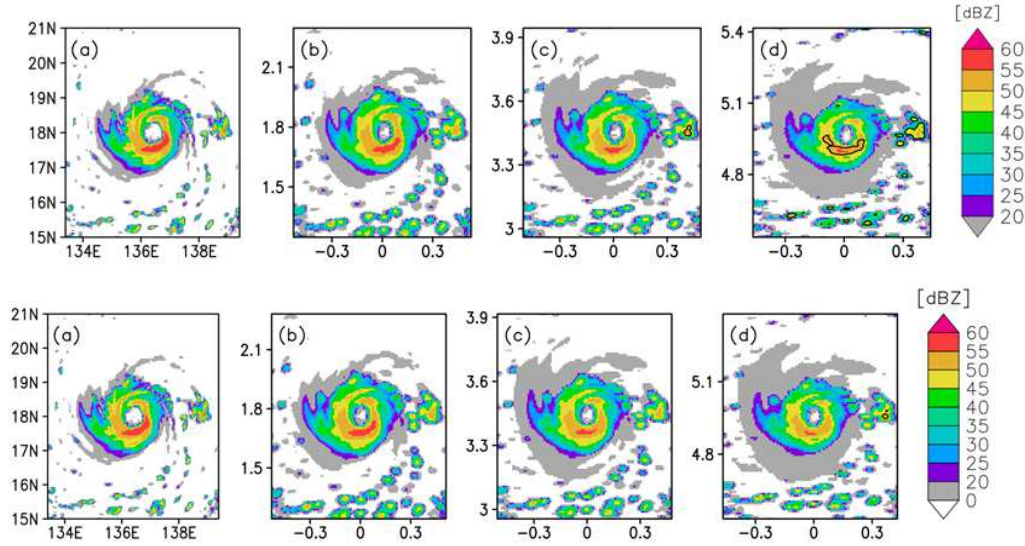
Figure 11 Precipitation reflectivity (dBZ) measured with bw20bs05 for the typhoons whose center is in (b) 10°N, (c) 20°N, and (d) 30°N. Contour in (b-d) corresponds to the area SCR > 0. Panel (a) shows the truth. ~~Note that the areas~~The area where reflectivity ~~form~~from precipitation ~~larger~~less than 0 dBZ are ~~shaded~~left blank.
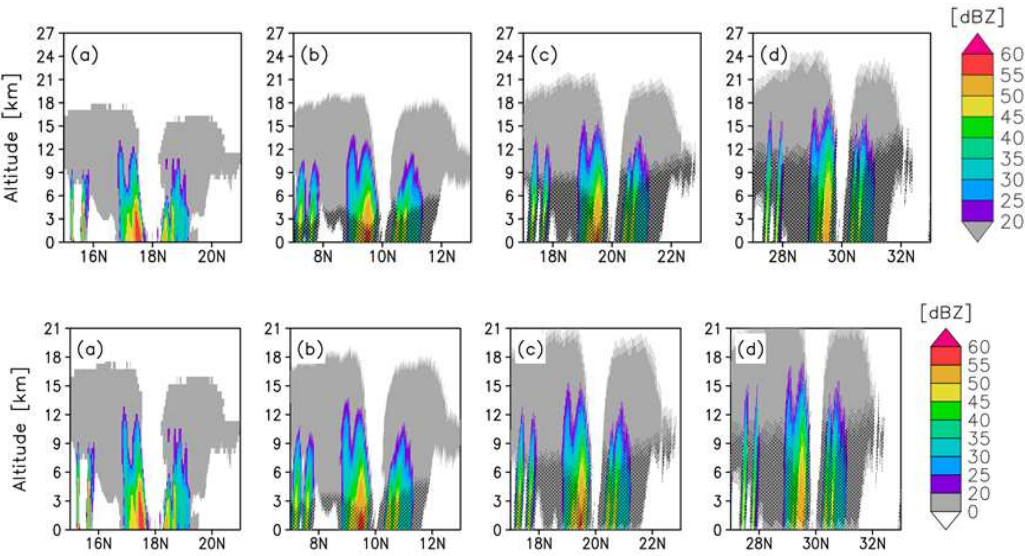
Figure 12 Precipitation reflectivity (dBZ) along 136.4°E longitude line passing through the typhoon

center measured with bw20bs05 for the typhoons whose center is in (b) 10°N, (c) 20°N, and (d) 30°N. ~~The area in which SCR < 0 is hatched in (b-d).~~ Panel (a) shows the truth. ~~Note that the areas~~ The area where reflectivity ~~form~~from precipitation ~~larger~~less than 0 dBZ are ~~shaded.~~left blank and the area in which SCR < 0 is hatched in (b-d).
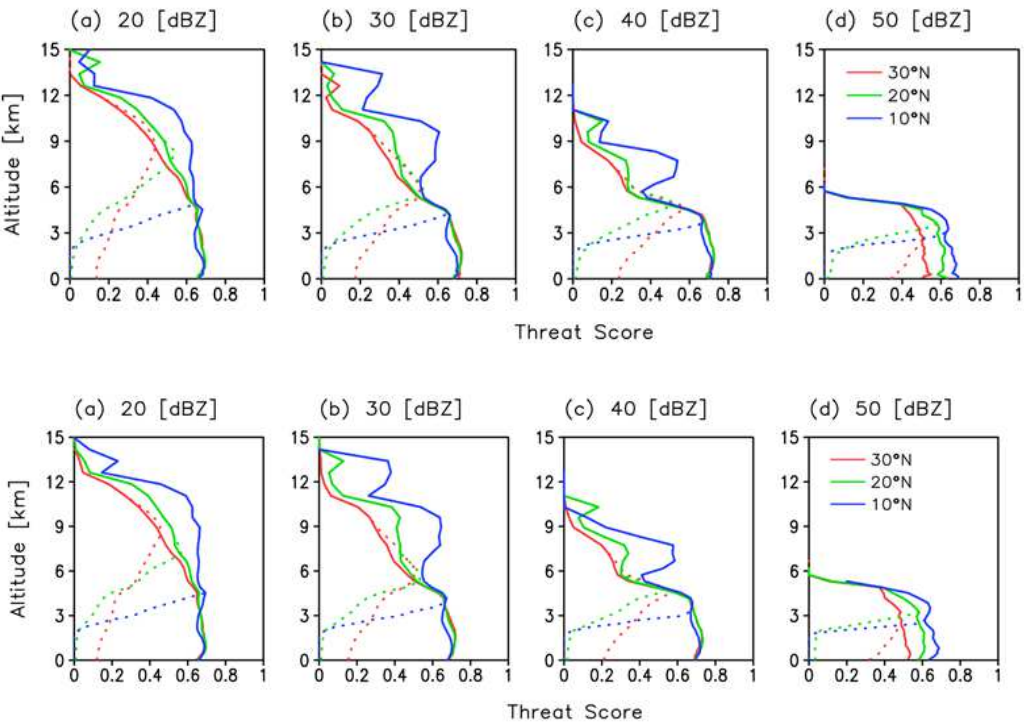
Figure 13 Threat score with a threshold of (a) 20, (b) 30, (c) 40, and (d) 50 (dBZ) for the typhoons whose centers are at 30°N (red), 20°N (green), and 10°N (blue). The dotted and solid lines show the threat score with and without considering the impact of surface clutter, respectively.
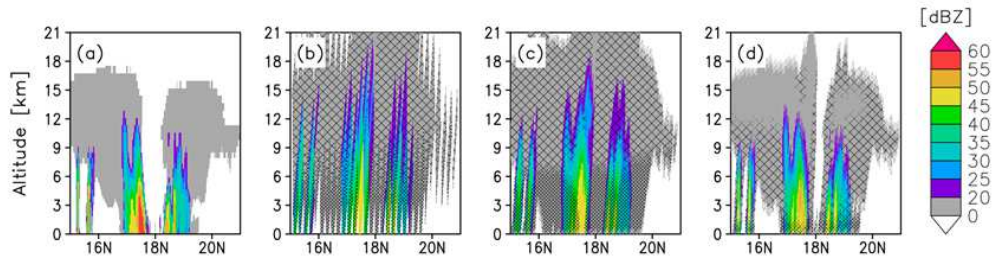
Figure 14 Precipitation reflectivity (dBZ) along 136.4°E longitude line passing through the typhoon center in the mature stage (0000 UTC, 5 August 2015) for (a) the truth, (b) bw20bs20, (c) bw20bs05, and (d) bw05bs05. The area where reflectivity from precipitation less than 0 dBZ are left blank and the area affected (SCR<0) by main lobe (sidelobe) clutter is densely (sparsely) hatched in (b-d).
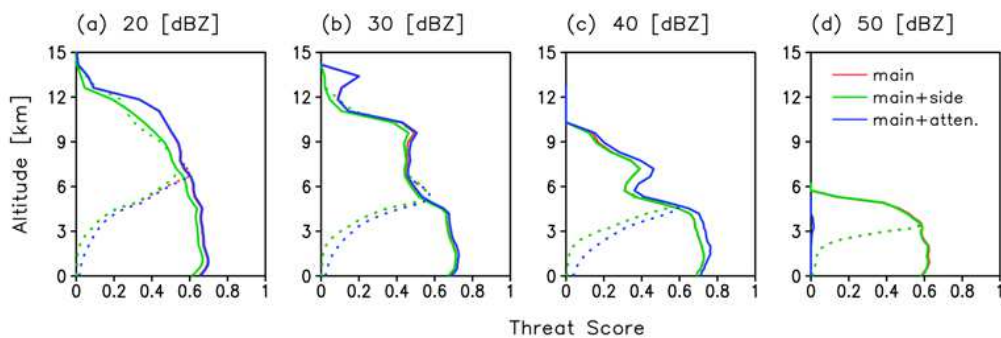
Figure 15 Threat scores with thresholds of (a) 20, (b) 30, (c) 40, and (d) 50 (dBZ) for bw20bs05. Red line overlaps blue line for (a), (b), and (c) and green line for (d). The dotted and solid lines show the threat score with and without considering the impact of surface clutter, respectively.